



Available online at [www.sciencedirect.com](http://www.sciencedirect.com)

**ScienceDirect**

*Acta Materialia* 66 (2014) 360–369



[www.elsevier.com/locate/actamat](http://www.elsevier.com/locate/actamat)

# Simulation of grain growth and sintering process by combined phase-field/discrete-element method

Kazunari Shinagawa\*

*Department of Advanced Materials Science, Faculty of Engineering, Kagawa University, Takamatsu, Kagawa 761-0396, Japan*

Received 6 September 2013; received in revised form 4 November 2013; accepted 6 November 2013

Available online 5 December 2013

## Abstract

A combination of the phase-field method (PFM) and the discrete-element method (DEM) is proposed to simulate simultaneously the movement of particles and the grain growth behavior in powder compacts during sintering. To take the mutual interaction into consideration, a precise way of coupling PFM and DEM is developed based on a sintering model. The sintering forces and the contact areas in linked particles are evaluated from the phase field variables, computed in PFM and introduced into the calculation of the rigid motion of particles in DEM. Before treating actual problems as the application, the sintering process of two particles is simulated first for fundamental verification, including the case with different particle sizes. It is confirmed that the changes in the neck size and the center-to-center distance between particles are reproduced well using the proposed method. Secondly, the simulation of microstructural evolution during sintering is implemented for some small clusters of particles. The internal spatial structure and the outer shape of the clusters vary with the shrinkage deformation as well as the grain boundary migration in sintering. The proposed method of simulating the microstructural evolution in sintering bodies may be effective in the computer-aided design of microscale components or thin films produced by powder processing.

© 2013 Acta Materialia Inc. Published by Elsevier Ltd. All rights reserved.

**Keywords:** Sintering; Phase-field method; Discrete-element method; Grain growth; Densification

## 1. Introduction

Current analytical methods of the sintering process can be divided into three levels – atomic, particle and continuum [1,2] – but may also be roughly categorized into two groups from the viewpoint of the target. One is the group for calculating distortion and stress in the sintering body; the other is suitable for simulating microstructural evolution, such as grain growth. For analyzing macroscopic deformation behavior of powder compacts during sintering, the finite element method (FEM) has been used as a common numerical technique for treating continuum [3]. On the other hand, the discrete-element method (DEM) has recently been used for the simulation of the sintering shrinkage behavior of powder compacts [4–14]. This has

the advantage of taking a network structure of particles directly into consideration. It is difficult for current workstations to treat industrial parts with normal size, but the application of DEM to the components of microscale devices may be possible. Conversely, DEM may be a suitable tool for computing deformation behavior of microscale components, because it is critically affected by each particle motion when the powder compacts consist of a small quantity of particles, that is, no longer a continuum. The grain boundary migration, however, cannot be dealt with in DEM itself, though the grain growth is an important phenomenon in the sintering process that affects the shrinkage as well as the microstructure of the components.

For the simulation of grain growth, the Monte Carlo method is commonly used, and applied to the sintering process [15,16]. Although the phase-field method (PFM) has also been applied to it recently [17–19], as a new numerical technique, there remains the problem of how

\* Tel.: +81 87 864 2404.

E-mail address: [shina@eng.kagawa-u.ac.jp](mailto:shina@eng.kagawa-u.ac.jp).

to deal with the rigid motion of particles during the initial and intermediate stages of sintering. Since it may be difficult to perform the computation for sintering shrinkage within the scheme of PFM itself, the author has proposed a combined phase-field/discrete-element method to simulate simultaneously the movement of particles and the grain growth behavior in powder compacts during sintering [20]. However, the link-up from PFM to DEM was not considered in this primary study with a simplified sintering model, where the conjugate force in sintering, namely the sintering force, was set to be constant, and the contact area between particles was given by a simple function of the center-to-center distance.

In the present study, a complete way of coupling PFM and DEM is proposed based on a precise sintering model. The sintering forces and the contact areas in linked powder particles are evaluated from the phase field variables, computed in PFM and taken into consideration in the calculation of the rigid motion of particles in DEM. Before treating actual problems as the application, the sintering process of two particles is simulated first for fundamental verification, including the case with different particle sizes. The validity of the calculated results is examined based on a classical model for the early stage of sintering, as a reference. Secondly, the simulations of the sintering process are implemented for some small clusters of particles, as a first step of applied problems, and each motion of the particles is confirmed.

## 2. Numerical methods

### 2.1. Phase-field method

Grain growth behavior with advection flux was described by Wang [18], based on the Cahn–Allen equations [21]:

$$\frac{\partial S_k}{\partial t} = -L \frac{\delta G}{\delta S_k} - \nabla \cdot \vec{J}_s \quad (1)$$

where  $S_k$  is the phase-field variable,  $t$  is the time,  $L$  is the constant characterizing grain boundary mobility,  $G$  is the total free energy and  $\vec{J}_s$  is the advection flux. The subscription  $k$  of  $S_k$  denotes the different crystallographic orientations of grains ( $k = 1, 2, \dots, p$ ).  $S_k$  is equal to 1 or -1 inside the grain and 0 outside it, with orientation  $k$ , and is taken to have intermediate values at the grain boundaries. For the conservation of mass, a relative density field is also treated based on the Cahn–Hilliard diffusion equation [22]:

$$\frac{\partial \rho}{\partial t} = \nabla \cdot \left( B \nabla \frac{\delta G}{\delta \rho} - \vec{J}_r \right) \quad (2)$$

where  $\rho$  is the relative density,  $B$  is the constant characterizing surface mobility and  $J_r$  is the advection flux. The total free energy  $G$  is assumed to be expressed as

$$G = \int \left\{ G_0 + \frac{\alpha}{2} (\nabla \rho)^2 + \sum_{k=1}^p \frac{\beta}{2} (\nabla S_k)^2 \right\} dV \quad (3)$$

$$G_0 = -\frac{a_1}{2} \left( \rho - \frac{1}{2} \right)^2 + a_1 \left( \rho - \frac{1}{2} \right)^4 + \frac{2a_3 - a_2}{4} \rho^4 + \sum_{k=1}^p \left\{ \frac{a_2}{2} (\rho - 1)^2 S_k^2 - \frac{a_3}{2} \rho^2 S_k^2 + \frac{a_4}{4} S_k^4 + \frac{a_5}{4} \sum_{l \neq k} S_k^2 S_l^2 \right\} \quad (4)$$

where  $G_0$  is the local free energy density (Appendix A),  $\alpha$  and  $\beta$  are gradient coefficients and  $a_1$ – $a_5$  are constants [17]. The calculation of Eqs. (1) and (2) is implemented by using the two-dimensional (2-D) finite difference method (FDM).

### 2.2. Discrete-element method

For the calculation of DEM, a model proposed by Parhami and McMeeking [6] is employed, but a 2-D version is used to meet the 2-D phase-field simulation. The transfer and the rotation of each particle are given by

$$\{f\} = [C]\{v\} + \{f_s\} \quad (5)$$

$$\{f\} = \{f_n^1 \ f_t^1 \ M^1 \ f_n^2 \ f_t^2 \ M^2\}^T \quad (6)$$

$$\{v\} = \{v_n^1 \ v_t^1 \ \dot{\theta}^1 \ v_n^2 \ v_t^2 \ \dot{\theta}^2\}^T \quad (7)$$

$$\{f_s\} = \{f_s^1 \ 0 \ 0 \ f_s^2 \ 0 \ 0\}^T \quad (8)$$

The components of  $\{f\}$  are the conjugate forces and the moments at the nodes of each element, where  $f_n$  and  $f_t$  are the normal and the tangential forces, respectively,  $M$  is the moment and superscript 1 or 2 is to make the distinction between adjoining particles.  $\{v\}$  contains the velocities and the rotational rate of the nodes corresponding to the forces and the moments, where  $v_n$ ,  $v_t$  are the normal and the tangential velocities, respectively, and  $\dot{\theta}$  is the rotational rate.  $\{f_s\}$  is the sintering force vector, which produces the rigid motion of particles, where  $f_s^1$  and  $f_s^2 (= -f_s^1)$  are the normal forces acting between particle 1 and 2. Matrix  $[C]$ , correlating  $\{f\}$  with  $\{v\}$ , is formulated as follows:

$$[C] = \begin{Bmatrix} a & 0 & 0 & -a & 0 & 0 \\ 0 & b & \frac{bl}{2} & 0 & -b & \frac{bl}{2} \\ 0 & \frac{bl}{2} & \frac{bl^2}{4} + c & 0 & -\frac{bl}{2} & \frac{bl^2}{4} - c \\ -a & 0 & 0 & a & 0 & 0 \\ 0 & -b & -\frac{bl}{2} & 0 & b & -\frac{bl}{2} \\ 0 & \frac{bl}{2} & \frac{bl^2}{4} - c & 0 & -\frac{bl}{2} & \frac{bl^2}{4} + c \end{Bmatrix} \quad (9)$$

where  $l$  is the center-to-center distance of the particles and  $a$ ,  $b$ ,  $c$  are parameters derived by a classical sintering model for grain boundary diffusion as follows:

$$a = \frac{2X^3}{3D_{gb}}, \quad b = 2X\eta, \quad c = \frac{2X^5}{45D_{gb}} \quad (10)$$

where  $X$  is the half width of neck,  $\overline{D}_{gb}$  is the effective grain boundary diffusivity and  $\eta$  is the tangential drag coefficient (Appendix B).

### 2.3. Coupling

The strategy of transferring the rigid motion from DEM to PFM, at every time step in the iterative computation, is as follows [20]. First, the velocity  $\vec{v}$  of a particle  $i$ , calculated in DEM, is converted into vector variables  $\{\vec{v}_k^i\}$ , corresponding to all crystallographic orientations  $k$ . Then, summing up the products of the phase-field variable  $S_k$  multiplied by  $\{\vec{v}_k^i\}$  for all surrounding particles gives the advection fluxes in Eqs. (1) and (2):

$$\vec{J}_s = \sum_{i=1}^n S_k \vec{v}_k^i \quad (11)$$

$$\vec{J}_r = \sum_{i=1}^n \rho \vec{v}_k^i \approx \sum_{i=1}^n S_k^2 \vec{v}_k^i \quad (12)$$

where  $n$  is the number of the particles in the vicinity of the particle  $i$ . In the present study, to consider the case that the particles rotating in clusters are non-circular, the correction due to the rotational rate  $\dot{\theta}$  is added to  $\vec{v}$  at each position of grid points in PFM:

$$\vec{v} = (V_x - \delta_x \dot{\theta}, \quad V_y + \delta_y \dot{\theta}) \quad (13)$$

where  $V_x$  and  $V_y$  are the original components of velocity and  $\delta_x$  and  $\delta_y$  are the distances from the center of the particle  $i$  to the position in the  $x$  and  $y$  direction, respectively.

On the other hand, from PFM to DEM, the neck size and the sintering force are returned. The area  $A$  of the grain boundary zone can be calculated by counting the number of grid points with  $S_i S_j > 0.05$ , as demonstrated in Fig. 1a. Dividing  $A$  by the grain boundary thickness  $d_{gb}$  gives the neck width  $2X = A/d_{gb}$ . Note that the grain boundary described in PFM is not sharp, and the thickness of the grain boundary zone is much larger than that of the real grain boundary width. As shown in Fig. 1b, in preparation for evaluating the sintering force from phase-field variables, the curvature  $\kappa_s$  and the unit normal vector  $\vec{n}$  of the surface are calculated by the change in phase-field variables with position, as follows:

$$\kappa_s = \nabla \cdot \vec{n} = \frac{\rho_{xx} \rho_y^2 - 2\rho_x \rho_y \rho_{xy} + \rho_{yy} \rho_x^2}{(\rho_x^2 + \rho_y^2)^{3/2}} \quad (14)$$

$$\vec{n} = \frac{\nabla \rho}{|\nabla \rho|} = \frac{1}{(\rho_x^2 + \rho_y^2)^{1/2}} (\rho_x, \rho_y) \quad (15)$$

where the subscripts denote partial derivative.

The sintering force has two terms as illustrated in Fig. 2. The first term is the sum of the surface tension multiplied by the curvature at each grid point  $j$  within a prescribed surface zone ( $0.1 < \rho < 0.7$ ):

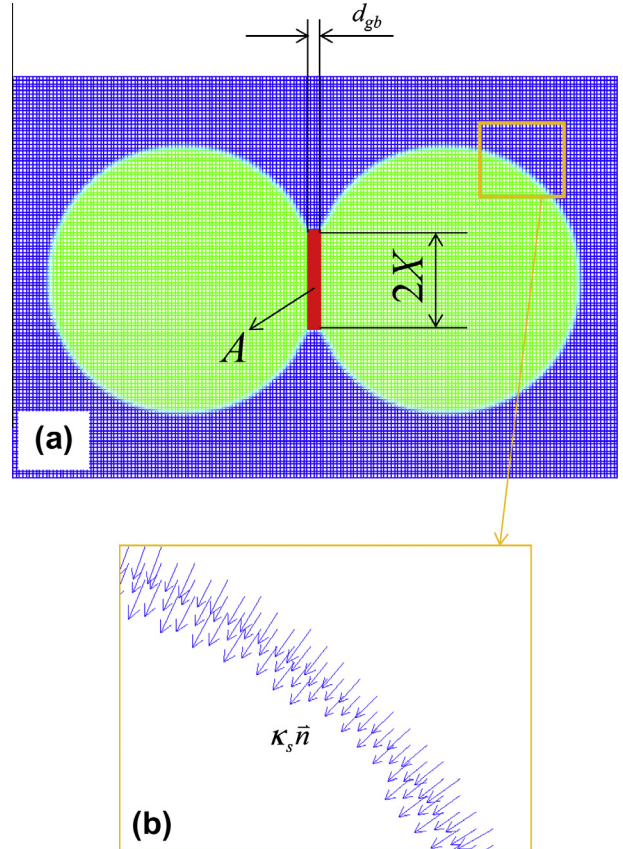


Fig. 1. Factors to transfer from PFM to DEM: (a) neck half width  $X$  calculated from area  $A$  and thickness  $d_{gb}$  of grain boundary zone ( $S_i S_j \geq 0.05$ ), (b) curvature  $\kappa_s$  and unit normal vector  $\vec{n}$  of surface zone ( $0.1 < \rho < 0.7$ ).

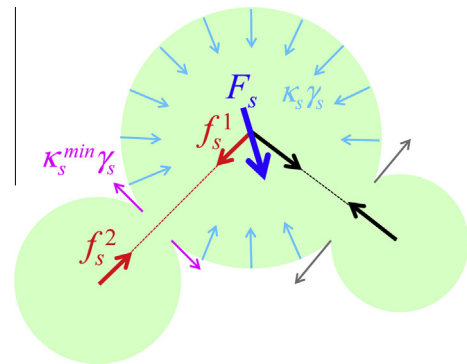


Fig. 2. Schematic for two terms of sintering force.

$$F_{si} = \frac{s}{N} \sum_j^N \kappa_{sj} \gamma_s n_i \quad (16)$$

where  $\gamma_s$  is the surface tension,  $n_i$  is the direction cosine,  $i = x, y$  and  $N$  is the number of grid points in the surface zone.  $s$  is a correction factor ( $s = 0.826$ ), which is determined by adjusting  $F_{sx}$  to  $2\gamma_s$  in the case of a lower semicircular surface. If there is no contact, this term is zero. Since a particle has a lot of contacts actually, this force is

introduced as the resultant force with all contacts taken into consideration:

$$\begin{Bmatrix} F_x \\ F_y \end{Bmatrix} = \begin{Bmatrix} 1 & 0 & 1 & 0 \\ 0 & 1 & 0 & 1 \end{Bmatrix} \begin{Bmatrix} f_{nx} \\ f_{ny} \\ f_{tx} \\ f_{ty} \end{Bmatrix} + \begin{Bmatrix} F_{sx} \\ F_{sy} \end{Bmatrix} \quad (17)$$

The second term of the sintering force arises from the stress at the neck tip  $\kappa_s^{\min} \gamma_s$ , which is the outward-directed traction. This traction is converted into the compressive normal force acting on the contact:

$$f_s = 2X\kappa_s^{\min} \gamma_s \quad (18)$$

and substituted into Eq. (8) as an imaginary force acting on each pair of particles. These two terms in sintering force correspond to those obtained from the classical model ([Appendix B](#)).

#### 2.4. Conditions of simulation

Fundamental simulations for sintering of two particles are performed for five pairs, as shown in [Table 1](#), where the equivalent radius  $R^*$  for different size  $R_1$  and  $R_2$  is evaluated by  $R^* = 2R_1R_2/(R_1 + R_2)$ . Since the grain boundary sliding does not occur in the two-particle model, the tangential drag coefficient  $\eta$  in Eq. (10) has no effect on the calculation, but a large value is input for the sake of convenience. The particle clusters, as an applied problem, consist of 4 and 10 particles, as shown in Nos. 6 and 7 of [Table 1](#) as well as in [Fig. 3](#). In this case, extremely small values of  $\eta$  are also set to examine how the grain boundary sliding works during sintering of clusters. The effective grain boundary diffusivity  $\bar{D}_{gb}$  is taken to be a small value, compared with the two-particle model, to reduce the sintering rate of unstable structures.

The other parameters used in the simulations are listed in [Table 2](#). For comparison, the phenomenological laws for various velocities on sintering and the equivalent equations in the present method are listed in [Table 3](#). Since the equations  $v_n$  and  $v_t$  for DEM, concerning the movement of particles, are originally derived from the phenomenological laws, as explained in [Appendix B](#), the constants  $\bar{D}_{gb}$  and  $\eta$  used in DEM are common, where  $\bar{D}_{gb}(=D_{gb}w_{gb}\Omega/k_B)$  is a function of the grain boundary diffusion coefficient  $D_{gb}$  with

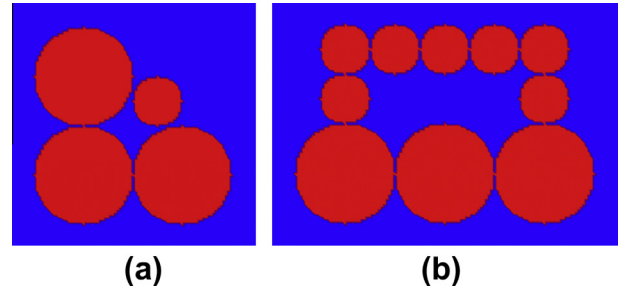


Fig. 3. Clusters for implementing simulation: (a) Cluster 1 and (b) Cluster 2.

Table 2

Parameters used in calculation.

Constant characterizing surface mobility $B$	1
Constant characterizing grain boundary mobility $L$	1
Gradient coefficient related to surface energy $\alpha$	3
Gradient coefficient related to grain boundary energy $\beta$	3
Constants in $G_0$ related to surface energy $a_1$	0.5
Constants in $G_0$ related to surface energy $a_2$	0.6
Constants in $G_0$ related to grain boundary energy $a_3$	1.2
Constants in $G_0$ related to grain boundary energy $a_4$	1.0
Constants in $G_0$ related to grain boundary energy $a_5$	4.0
Surface tension $\gamma_s$ (for DEM)	0.40
Thickness of grain boundary $d_{gb}$ (for DEM)	10.6

Table 3

Phenomenological laws for various velocities and equivalent equations in PFM/DEM.

Velocity	Law	Equivalent equation	
G.B. migration $v_b$	$\bar{D}_a \kappa_{gb} \gamma_{gb}$	$L \kappa_{gb} \beta$	(PFM)
Motion by surface diffusion $v_s$	$\bar{D}_s \nabla^2 \kappa_s \gamma_s$	$B \nabla^2 \kappa_s \alpha$	(PFM)
Shrinkage due to G.B. diffusion $v_n$	$\frac{3\bar{D}_{gb}}{X^2} (\bar{\sigma} - \sigma_t)$	$\frac{3\bar{D}_{gb}}{2X^3} (F_n - F_s)$	(DEM)
G.B. sliding $v_t$	$\frac{\tau}{\eta}$	$\frac{F_t}{2X\eta}$	(DEM)

the grain boundary width  $w_{gb}$ , the atomic volume  $\Omega$ , the Boltzmann constant  $k_B$  and the temperature  $T$ . In the phenomenological law for interface migration, as is well known, the velocity is assumed to be a product of the driving force and the mobility. For the grain boundary migration, the velocity  $v_b$  can be expressed by the driving force  $\kappa_{gb} \gamma_{gb}$  and the mobility  $\bar{D}_a$  ( $\approx D_a \Omega / w_{gb} k_B T$ ), where  $D_a$  is the diffusion coefficient for atomic motion across the grain boundary [23]. The velocity  $v_s$  of the motion by the surface

Table 1  
Conditions of calculation.

No.	Model	Number of particles	Grid points	$R$	$\bar{D}_{gb}$	$\eta$
1	Pair	2	180 × 120	80	100	10,000
2	Pair	2	180 × 120	60	100	10,000
3	Pair	2	180 × 120	40	100	10,000
4	Pair	2	180 × 120	80 & 60 (68.6 <sup>a</sup> )	100	10,000
5	Pair	2	180 × 120	80 & 40 (53.3 <sup>a</sup> )	100	10,000
6	Cluster	4	200 × 200	80 & 40	20	1, 0.01
7	Cluster	10	280 × 200	80 & 40	20	40, 5

<sup>a</sup> Equivalent radius.

diffusion also includes  $\kappa_s \gamma_s$  and  $\bar{D}_s (= D_s w_s \Omega / k_B T)$ , where  $D_s$  is the surface diffusion coefficient and  $w_s$  is the width of the surface [24]. On the other hand, the equivalent equations  $v_b$  and  $v_s$  for PFM, indicated in the right-hand side of Table 3, are derived by the sharp-interface approach (Appendix C). As pointed out by Allen and Cahn [21] and others [25,26], these equations are functions of the gradient coefficients ( $\alpha, \beta$ ), but not the interfacial energy ( $\gamma_s, \gamma_{gb}$ ), that is,  $v_b$  and  $v_s$  for PFM are not specifically equivalent to the phenomenological laws. Under certain assumptions, it may be possible to coordinate  $L$  and  $B$  with  $D_{gb}$  through the ratio to  $D_a$  and  $D_s$ , but the simple values of  $L = B = 1$  as well as  $a = \beta = 3$  are employed in the present study.

The calculations of PFM are conducted by using FDM, as previously explained. As the conditions for FDM, the numbers of the grid points are indicated in Table 1. The grid size is set to be  $\Delta x = \Delta y = 2.0$ , and the time increment of  $\Delta t = 0.1$  is employed. In the aforementioned method of coupling, the thickness of the grain boundary zone  $d_{gb}$  and the surface energy  $\gamma_s$  are required for evaluating the neck width and the sintering force for DEM.  $d_{gb}$  and  $\gamma_s$  are theoretically estimated to be  $d_{gb} = 6.5$  and  $\gamma_s = 0.55$  from the parameters  $a_3, a_4, a_5, \beta$  with Eqs. (A.4) and (A.6b), and  $a_1, a_2, \alpha$  with Eqs. (A.2) and (A.5a), respectively, as the sharp-interface limits [25] (Appendix A). The actual grain boundary thickness, however, is settled into an enlarged value depending on the numerical integration with a certain grid size in FDM. From a preliminary calculation of the grain boundary zone of  $S_i S_j > 0.05$  in FDM with  $\Delta x = 2.0$ , an appropriate value to give the correct neck width, defined by  $\rho > 0.8$ , was found to be  $d_{gb} = 10.6$ , which is employed for DEM as indicated in Table 2. The actual surface energy  $\gamma_s$  can also be directly evaluated from the data of FDM by

$$\gamma_s = 3 \sum_i \frac{\alpha}{2} \left( \frac{\Delta \rho_i}{\Delta x} \right)^2 \Delta x \quad (19)$$

where  $\Delta \rho_i (= \rho_{i+1} - \rho_i)$  is the increment in  $\rho$  at the  $i$ th grid point in a line intersecting a straight surface. In the preliminary calculation,  $\gamma_s = 0.40$  was obtained, and this value is used for DEM.

## 2.5. Reference model

As a reference, a 2-D model for the early stage of sintering is prepared for cylindrical particles. Based on a conventional geometric approximation in two-sphere model (Appendix D), the relationship between the curvature at the neck tip and the neck width is assumed to be given by

$$K_s^{\min} = \frac{2R}{X^2} \quad (20)$$

and the relationship between the shrinkage and the neck size of cylinders can be approximated by

$$\frac{\Delta l}{l_0} = \frac{1}{5} \left( \frac{X}{R} \right)^2 \quad (21)$$

where  $R$  is the radius of particles and  $l_0$  is the initial distance of the particles. The increase in neck size with time is expressed as

$$\left( \frac{X}{R} \right)^6 = \frac{45 \bar{D}_{gb} \gamma_s}{R^4} t \quad (22)$$

from a classical sintering model (Appendix E). The shrinkage with time is given by Eqs. (21) and (22) as follows:

$$\left( \frac{\Delta l}{l_0} \right)^3 = \frac{9}{25} \frac{\bar{D}_{gb} \gamma_s}{R^4} t \quad (23)$$

## 3. Results and discussion

### 3.1. Two-particle model

Fig. 4 shows some examples of the shape changes calculated in the simulations for sintering of the particle pairs. The particles in Fig. 4b No. 3 shrank faster than those in Fig. 4a No. 1, because the size effect was transferred into the advection flux in PFM as the difference in approaching rate through the sintering force in DEM. In the case of Fig. 4c No. 5, for a pair of large and small particles, the grain boundary migration occurred after the neck growth, and then the smaller particle disappeared finally. The surface profiles shown in Fig. 4 are similar to but different from those obtained in PFM by Asp and Ågren [19], where the approach between particles due to the rigid motion was not taken into consideration. The qualitative nature of sintering behavior in the two-particle model can be well reproduced by the proposed method. The quantitative point of view is discussed below with the classical model of Eqs. (20)–(23).

The change in radius of curvature at the neck tip obtained from the simulation is shown in Fig. 5a, where the lines calculated by the approximate equation, Eq. (20), and the original expression, Eq. (D.4), for the geometric model, are also superimposed. The radii of curvature obtained from the simulation increased in the range of  $X/R < 0.5$  as described by Eq. (20), but tended to become constant in the later stage. The approximate expression, Eq. (20), departs from the original expression, Eq. (D.4), around  $X/R = 0.4$ , but the simulated results show smaller radii of curvature than that calculated by Eq. (D.4), itself in the range of  $X/R > 0.4$ . This may be because the dihedral angle in the equilibrium state of the phase-field is  $\sim 120^\circ$  under the current conditions, though the dihedral angle for Eq. (D.4) in the classical model with circular neck is equivalent to  $180^\circ$ . The reason why the lines normalized by  $R$  for three different particle sizes did not show the same trajectory in the graph may be because the numerical differentiation to obtain curvature was affected by the grid size. On the other hand, the relationship between the shrinkage and the neck half width was in good agreement with the approximate expression, Eq. (21), for the geometric model, as shown in Fig. 5b, including the cases of Nos. 4 and 5,

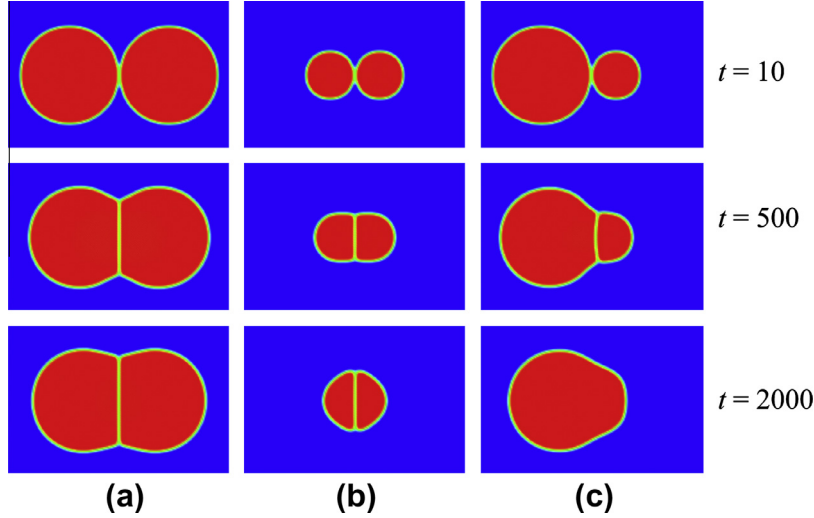


Fig. 4. Deformation of two particles with sintering time  $t$  ( $\bar{D}_{gb} = 100$ ): (a) No. 1, (b) No. 3 and (c) No. 5.

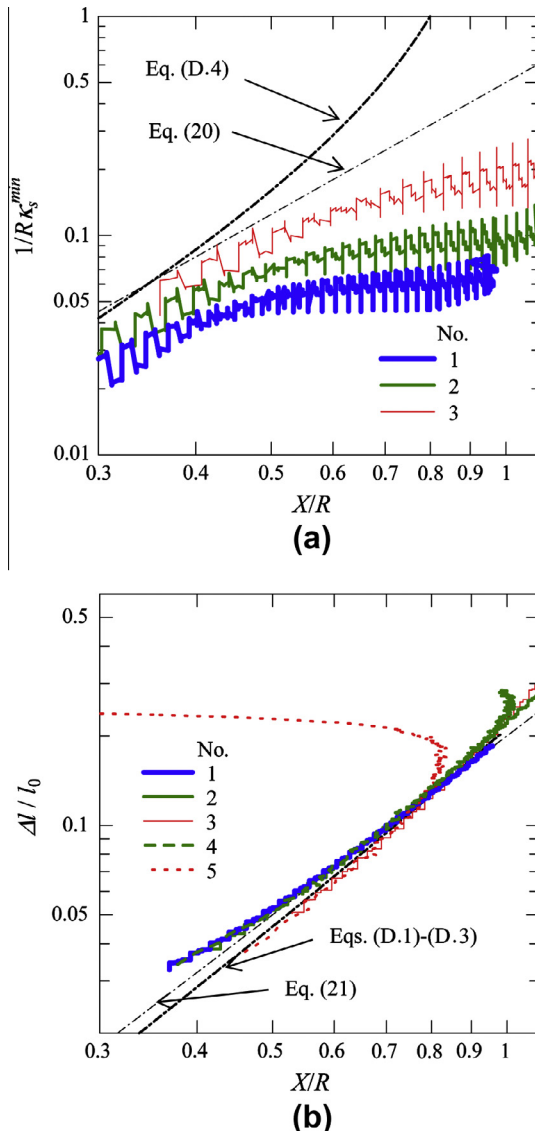


Fig. 5. Change in geometry of two-particle model: (a) radius of curvature at neck tip vs. neck half width and (b) shrinkage vs. neck half width.

where the smaller particle shrinks due to the grain boundary migration. As for the initial center-to-center distance  $l_0$ , a value 2% larger than  $2R$  was employed, because the neck already existed at  $l_0 = 2R$  due to the formation of the interface zone in the phase-field model. Note that the line of Eq. (21) approximates well the original numerical result with Eqs. (D.1)–(D.3), in the whole range in Fig. 5b.

Fig. 6 shows the time dependence of dimensional change in the two-particle model. The lines of the change in neck half width as well as shrinkage with time in the simulation lie superior to those of Eqs. (22) and (23), respectively. Since the change in neck size follows Eq. (21), as explained for Fig. 5b, and the same viscous response as the classical sintering model is exactly introduced into DEM through Eq. (10), the discrepancy in rate of the geometric change principally comes from the difference in the sintering force. As for the sintering stress, the value of Eq. (18) is large compared with Eq. (16), and thus the value of curvature at the neck tip may be dominant. Since the curvatures calculated in PFM were larger than that given by Eq. (20) for the sintering model, the neck growth and the shrinkage rate also became larger.

When the three-dimensional (3-D) version of the present model is developed, the comparisons with the other models will become possible. Numerical simulations for sintering two spheres by treating both grain boundary and surface diffusion were conducted by Svoboda and Riedel [27], and also by Bouvard and McMeeking [28]. Furthermore, Pan and Cocks developed a method for simulating sintering processes with grain boundary migration [29] and an extended 3-D model [30]. Parhami et al. [31] also proposed a model for the sintering and coarsening of rows of spherical particles, by using the variational principle. The present combined method in the 3-D version can be compared with these models, but the comparisons will be done only for the limited conditions of the fast surface diffusion, because the surface profile calculated by the present model should be in the equilibrium state for each given

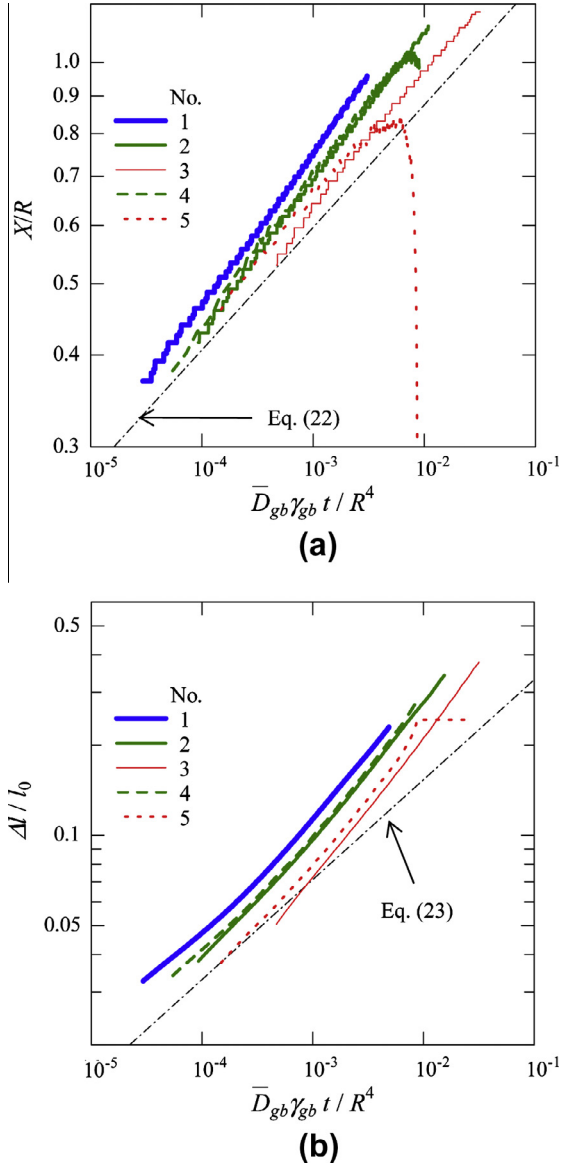


Fig. 6. Change in dimension with time in two-particle model: (a) neck half width and (b) shrinkage.

center-to-center distance. Since the process of lattice diffusion is not computed in PFM, it may be difficult to simulate the shrinkage behavior in the case of slow surface diffusion, even if the parameter related to surface migration  $B$  in Eq. (5) is set to be small. Nevertheless, the advantage that the sintering behavior of the network structure of particles can be simulated with the grain growth process may be useful. For the validation of the validity of the present model, the experimental work for the following cluster models will be done in the future.

### 3.2. Cluster models

Fig. 7 displays the shrinkage deformation and the grain boundary migration in Cluster 1, for  $\eta = 1.00$  (a) and 0.01 (b). As can be seen in Fig. 7a, the two large particles on

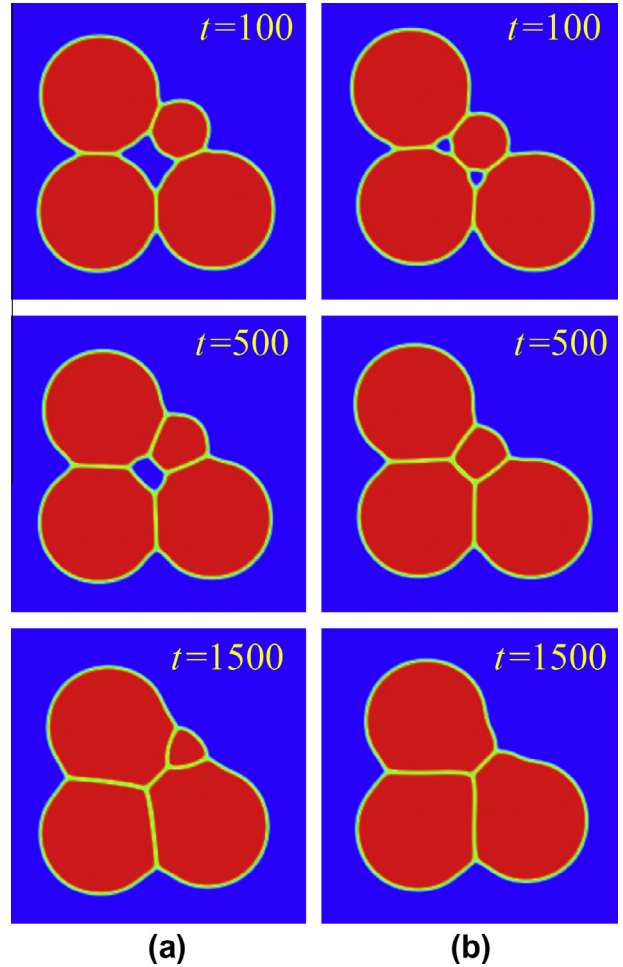


Fig. 7. Sintering behavior of Cluster 1 ( $\bar{D}_{gb} = 20$ ): (a)  $\eta = 1$  and (b)  $\eta = 0.01$ .

either side of the small particle came closer, because the sintering forces acting between small and large particles are larger than those between large particles. In the case of  $\eta = 0.01$ , shown in Fig. 7b, since the grain boundary sliding was enhanced, the small particle cut into the space between two large particles, and moved these two particles out of the way once. However, the size of the small particles was decreased by the grain growth process, and disappeared finally, which caused the approach of the two large particles later in the same way as Fig. 7a.

Fig. 8 demonstrates the sintering behavior of Cluster 2, for  $\eta = 40$  (a) and 5 (b). In the case of small grain boundary sliding with  $\eta = 40$ , a stable shape change was observed in spite of an unstable cluster structure, where the two small particles next to the large particles disappeared first by grain growth. On the other hand, with  $\eta = 5$ , small particles in the upper part of the cluster shrank strongly due to the large sintering force, and the cluster warped upward, followed by asymmetric distortion and grain growth.

It is confirmed that the present combined model makes it possible to calculate shrinkage behavior accompanied by grain growth, by implementing the simulation with cluster models, where the difference in sintering behavior affected

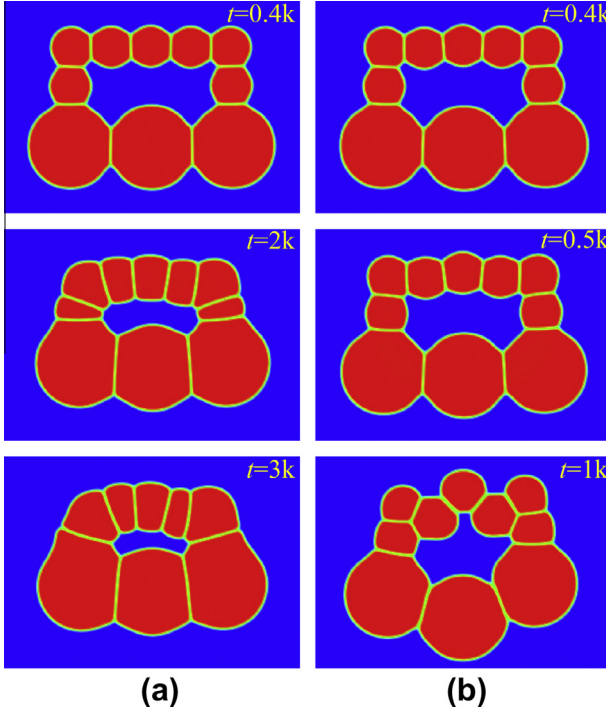


Fig. 8. Sintering behavior of Cluster 2 ( $\bar{D}_{gb} = 20$ ): (a)  $\eta = 40$  and (b)  $\eta = 5$ .

the internal spatial structure as well as the outer shape. A change in pore configuration in a particle cluster was simulated by Bruchon et al. [32], by using the level-set method for the process with surface and lattice diffusion, but without considering the shrinkage among particles. From the point of view of DEM, a simple attempt to consider grain growth has been done by Martin et al. [8], where the sizes of small and large particles on each side of the contact were changed by using the rate equation for grain growth. This kind of coarsening model is useful for simulating macroscopic behavior of powder compacts, but may not be enough to treat each particle. The present combined method can solve the problem related to both shrinkage distortion and grain growth in microscale components.

#### 4. Conclusions

A method of combining PFM and DEM was proposed to simulate grain boundary migration as well as shrinkage deformation during sintering of powder compacts. In this method, the rigid motion calculated by DEM is transferred to the advection flux in PFM. The sintering force needed in DEM is divided into the two terms related to the surface curvature of particles and the neck width. They are evaluated from the neck width and the curvature of surface in PFM, and introduced as the resultant force of a particle and the forces between particles, respectively. By introducing this sintering model into the formula in DEM, the sintering shrinkage and the neck growth behavior of two particles were well described. The simulations of sintering clusters were also demonstrated, and the shrinkage distortion and the grain growth behavior of each particle were

confirmed. The validity of the present method will be verified by comparison with experiment, after the 3-D version is developed. This method may be useful to predict shape, pore configuration and surface roughness in microstructural components.

#### Acknowledgements

This work was supported by Grants-in-Aid for Scientific Research (C) (No. 23560869) from the Japan Society for the Promotion of Science.

#### Appendix A. Parameters for free energy in PFM and sharp-interface limits

The local free energy density  $G_0$  expressed by Eq. (4) is illustrated as a 3-D profile with a single phase-field variable  $S_1$  in Fig. A.1. Thus the parameters  $a_1$ – $a_4$  are selected to create a potential energy surface having the minimum points at  $S_1 = 1$  (or  $-1$ ) for  $\rho = 1$  (crystalline and solid) and  $S_1 = 0$  for  $\rho = 0$  (non-crystalline and vapor), which lead to stable states. The parameter  $a_5$  is the factor of the double well potential to suppress the overlap of the grain ( $k = 1$ ) with the others ( $k \neq 1$ ). These parameters can be related to the interfacial energies by considering equilibrium conditions, i.e.  $\partial S_k / \partial t = \partial \rho / \partial t = 0$  for Eqs. (1) and (2). In these conditions, the phase field variables  $\rho$  and  $S_1$  in the  $x$ -direction around the surface of a grain ( $k = 1$ ) satisfy  $\alpha \cdot d^2 \rho / dx^2 = \partial G_0 / \partial \rho$  and  $\beta \cdot d^2 S_1 / dx^2 = \partial G_0 / \partial S_1$ , respectively. Integrating these equations with the boundary conditions: (1)  $d\rho / dx = dS_1 / dx = 0$  at  $x = \pm\infty$ , (2)  $\rho = S_1 = 0$  at  $x = \infty$ , (3)  $\rho = S_1 = 1$  at  $x = -\infty$ , (4)  $S_{k \neq 1} = 0$ , yield

$$\frac{\alpha}{2} \left( \frac{d\rho}{dx} \right)^2 = \frac{\beta}{2} \left( \frac{dS_1}{dx} \right)^2 = G_0 + \frac{a_1}{16} = \Delta G_0^s \quad (\text{A.1})$$

The first equality in Eq. (A.1) with the above boundary conditions (2) and (3) furthermore requires  $\alpha = \beta$ , which yields  $\rho = S_1$ , and settles the left-hand side of Eq. (A.1), that is, the energy barrier between solid and vapor:

$$\Delta G_0^s = \left( a_1 + \frac{a_2}{2} \right) \rho^2 - (2a_1 + a_2) \rho^3 + \left( a_1 + \frac{a_2}{2} \right) \rho^4 \quad (\text{A.2})$$

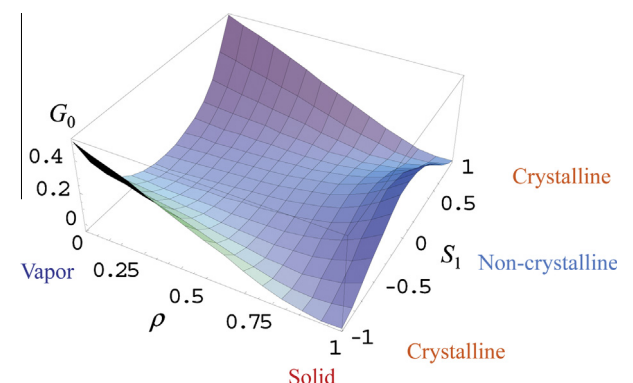


Fig. A.1. 3-D profile of local free energy density  $G_0$ .

Similarly, the phase field variables  $S_1$  and  $S_2$  in the  $x$ -direction around the grain boundary between two grains ( $k = 1$  and 2) satisfy  $\beta \cdot \partial^2 S_k / \partial x^2 = \partial G_0 / \partial S_k$ , respectively. Integrating these equations with the boundary conditions: (1)  $dS_k / dx = 0$  at  $x = \pm\infty$ , (2)  $S_1 = 0$ ,  $S_2 = 1$  at  $x = \infty$ , (3)  $S_1 = 1$ ,  $S_2 = 0$  at  $x = -\infty$ , (4)  $\rho = 1$  and  $S_{k \neq 1,2} = 0$ , yields

$$\frac{\beta}{2} \left( \frac{dS_1}{dx} \right)^2 = \frac{\beta}{2} \left( \frac{dS_2}{dx} \right)^2 = G_0 + \frac{a_1}{16} = \Delta G_0^{gb} \quad (\text{A.3})$$

The first equality in Eq. (A.3) with the above boundary conditions (2) and (3) yields  $S_2 = 1 - S_1$ , and settles the energy barrier in the grain boundary:

$$\begin{aligned} \Delta G_0^{gb} &= (a_3 - a_4)S_1 + \left( -a_3 + \frac{3}{2}a_4 + \frac{a_5}{4} \right)S_1^2 \\ &\quad - \left( a_4 + \frac{a_5}{2} \right)S_1^3 + \left( \frac{a_4}{2} + \frac{a_5}{4} \right)S_1^4 \end{aligned} \quad (\text{A.4})$$

Then the surface energy and the grain boundary energy can be obtained by using Eqs. (A.2) and (A.4), respectively, as follows [21]:

$$\gamma_s = 3\sqrt{\frac{\alpha}{2}} \int_0^1 \sqrt{\Delta G_0^s} d\rho \quad (\text{A.5a})$$

$$\gamma_{gb} = 3\sqrt{\frac{\beta}{2}} \int_0^1 \sqrt{\Delta G_0^{gb}} dS_1 \quad (\text{A.5b})$$

The thicknesses of the surface zone and the grain boundary zone are also estimated from

$$d_s = \sqrt{\frac{\alpha}{2}} \int_{-\zeta}^{1-\zeta} \frac{d\rho}{\sqrt{\Delta G_0^s}} \quad (\text{A.6a})$$

$$d_{gb} = \sqrt{\frac{\beta}{2}} \int_{-\zeta}^{1-\zeta} \frac{dS_1}{\sqrt{\Delta G_0^{gb}}} \quad (\text{A.6b})$$

where  $\zeta (\ll 1)$  denotes a range of the interface.

## Appendix B. Parameters for 2-D DEM

Parameters for 2-D DEM are derived based on a classical model for sintering with grain boundary diffusion. By considering the atom flux driven by the stress gradient on the contact of cylindrical particles as well as the mass conservation, the normal velocity of the contact ( $v_n = v_n^1 - v_n^2$ ) can be obtained as a differential equation:

$$v_n = -\bar{D}_{gb} \frac{\partial^2 \sigma}{\partial x^2} \quad (\text{B.1})$$

where  $\sigma$  is a normal stress on the contact and  $x$  is the coordinate in the contact. Solving this equation with boundary conditions  $\partial\sigma/\partial x = 0$  at  $x = 0$  and  $\sigma = \sigma_t$  at  $x = X$  gives

$$v_n = \frac{3\bar{D}_{gb}}{X^2} (\tilde{\sigma} - \sigma_t), \quad \tilde{\sigma} = \frac{1}{2X} \int_{-X}^X \sigma dx \quad (\text{B.2})$$

Since the relationship between stress and force is  $2X(\tilde{\sigma} - \sigma_t) = (F_n - F_s)$ , Eq. (B.2) can be rewritten as

$$v_n = \frac{1}{a} (F_n - F_s), \quad a = \frac{2X^3}{3\bar{D}_{gb}} \quad (\text{B.3})$$

Note that the sintering force  $-F_s = 2X(-\tilde{\sigma} + \sigma_t)$  is obtained under the condition of  $F_n = 0$  and  $v_n = 0$ . On the other hand, the tangential velocity of the contact ( $v_t = v_t^1 - v_t^2$ ) is assumed to be given by

$$v_t = \frac{\tau}{\eta} = \frac{1}{\eta} \frac{F_t}{2X} = \frac{1}{b} F_t, \quad b = 2X\eta \quad (\text{B.4})$$

where  $\tau$  is the tangential stress. When a particle is rotated by  $\dot{\theta} = \dot{\theta}^1 - \dot{\theta}^2$ , the normal velocity at each point on the contact  $\bar{v}_n$  is produced by an additional normal stress  $\bar{\sigma}$ :

$$\bar{v}_n = x\dot{\theta} = -\bar{D}_{gb} \frac{\partial^2 \bar{\sigma}}{\partial x^2} \quad (\text{B.5})$$

By solving this equation with boundary conditions  $\bar{\sigma} = 0$  at  $x = X$ , the distribution of  $\bar{\sigma}$ , due to the rotation of particle, is obtained:

$$\bar{\sigma} = \frac{\dot{\theta}}{6\bar{D}_{gb}} (-x^3 + X^2 x) \quad (\text{B.6})$$

Thus the moment  $M = M^1 - M^2$ , which causes the rotation, can be calculated by

$$M = \int_{gb} \bar{\sigma} x dx = \frac{2X^5}{45\bar{D}_{gb}} \dot{\theta} = c\dot{\theta}, \quad c = \frac{2X^5}{45\bar{D}_{gb}} \quad (\text{B.7})$$

## Appendix C. Parameters for mobility in PFM

Consider the curved grain boundary with radius of curvature of  $R_{gb}(t)$  moving in steady state, in the cylindrical coordinate system. The velocity of the grain boundary at  $r = R_{gb}$  can be expressed by the change in  $S_1$  at fixed  $r$  with constant gradient  $\partial S_1 / \partial r$  [21]:

$$v_{gb} = \frac{\partial R_{gb}}{\partial t} = - \left( \frac{\partial S_1}{\partial t} \right)_r / \left( \frac{\partial S_1}{\partial r} \right)_t \quad (\text{C.1})$$

In the equilibrium state of the grain boundary with  $\beta \cdot \partial^2 S_k / \partial r^2 = \partial G_0 / \partial S_k$  and  $J_s = 0$ , Eq. (1) becomes

$$\frac{\partial S_1}{\partial t} = L \frac{\beta}{r} \frac{\partial S_1}{\partial r} \quad (\text{C.2})$$

where  $\delta G / \delta S_k = \partial G_0 / \partial S_k - \beta(\partial^2 S_k / \partial r^2 + \partial S_k / r \partial r)$  is used. Applying Eq. (C.2) to Eq. (C.1) with  $r = R_{gb}$  gives  $v_{gb} = L\beta/R_{gb} = L\kappa_{gb}\beta$ , where  $\kappa_{gb}$  is the curvature of the grain boundary.

The velocity of the surface at  $r = R_s$  in steady state is also obtained by

$$v_s = \frac{\partial R_s}{\partial t} = - \left( \frac{\partial \rho}{\partial t} \right)_r / \left( \frac{\partial \rho}{\partial r} \right)_t \quad (\text{C.3})$$

Similarly, Eq. (2) becomes

$$\frac{\partial \rho}{\partial t} = -B\nabla^2 \frac{\alpha}{r} \cdot \frac{\partial \rho}{\partial r} \quad (\text{C.4})$$

and applying Eq. (C.3) to Eq. (C.4) with  $r = R_s$  gives  $v_s = B\nabla^2(\alpha/R_s) = B\nabla^2\kappa_s\alpha$ .

## Appendix D. 2-D geometric model

The relationships between geometric parameters in overlapping two cylindrical particles are formulated. When the overlap distance of the two particles with radius  $R$  is  $2h$ , the distance of the position of an intersection point between the two circles from the central axis  $x=0$  is  $X_0 = \sqrt{h(2R-h)}$ , and the area of an overlapping segment is given by

$$A_1 = \frac{h(3h^2 + 16X_0)}{6X_0} \quad (\text{D.1})$$

The area enclosed by the overlapping two circles and a circle of radius  $r_c$  tangential to them at the position of  $x = X_1$  can be expressed as follows:

$$A_2 = 2 \int_{X_0}^{X_1} \left\{ R - \sqrt{R^2 - x} - (X_1 - X_0)h \right\} dx - r_c^2 \left\{ \tan^{-1} \frac{X_1}{R} - \frac{X_1}{R} \sqrt{1 - \left( \frac{X_1}{R} \right)^2} \right\} \quad (\text{D.2a})$$

$$r_c = R \left( \frac{R - h}{\sqrt{R^2 - X_1^2}} - 1 \right) \quad (\text{D.2b})$$

$X_1$  is numerically calculated by equalizing  $A_1$  and  $A_2$ , as a function of  $h$ , and converted into  $X$  by

$$\frac{X}{R} = 1 + \left( 1 - \frac{1}{R} \right) \sqrt{\frac{R - X_1}{R + X_1}} \quad (\text{D.3})$$

The obtained relationship between  $X/R$  and  $h/R = \Delta l/l_0$  can be approximated as Eq. (21). The radius of curvature, normalized by  $R$ , is given by

$$\frac{1}{K_s^{\min} R} = \frac{r_c}{R} = \frac{(h/R)^2 - 2h/R + (X/R)^2}{2(1 - X/R)} \quad (\text{D.4})$$

and the first term after the series expansion of Eq. (D.4) is  $X^2/2R^2$ , which gives a classical linear approximate expression for the curvature at the neck tip, Eq. (20).

## Appendix E. 2-D sintering model

From Eq. (20), the stress at the neck tip in Eq. (C.2) is expressed by

$$\sigma_t = K_s^{\min} \gamma_s = \frac{2R\gamma_s}{X^2} \quad (\text{E.1})$$

Substituting Eq. (E.1) into Eq. (C.2) with an assumption of small contact ( $\tilde{\sigma} \approx 0$ ) gives

$$\frac{dl}{dt} = -v_n \approx -\frac{6\bar{D}_{gb}R\gamma_s}{X^4} \quad (\text{E.2})$$

By using Eq. (21), a differential equation for  $X$  is obtained as

$$\frac{dX}{dt} = \frac{5}{4} \frac{R}{X} \frac{dl}{dt} = \frac{15}{2} \frac{\bar{D}_{gb}R^2\gamma_s}{X^5} \quad (\text{E.3})$$

Solving Eq. (E.3) gives Eq. (22).

## References

- [1] Oleovsky EA. Mater Sci Eng R: Rep 1998;23:41.
- [2] Pan J. Int Mater Rev 2003;48:69.
- [3] Kraft T, Riedel H. J Eur Ceram Soc 2004;24:345.
- [4] Jagota A, Dawson PR. Acta Metall 1988;36:2563.
- [5] Jagota A, Scherer GW. J Am Ceram Soc 1995;78:521.
- [6] Parhami F, McMeeking RM. Mech Mater 1998;27:111.
- [7] Martin CL, Bouvard D, Delette G. J Am Ceram Soc 2006;89:3379.
- [8] Martin CL, Schneider LCR, Olmos L, Bouvard D. Scripta Mater 2006;55:425.
- [9] Henrich B, Wonisch A, Kraft T, Moseler M, Riedel H. Acta Mater 2007;55:753.
- [10] Wonisch A, Guillon O, Kraft T, Moseler M, Riedel H, Rödel J. Acta Mater 2007;55:5187.
- [11] Martin CL, Bordia RK. Acta Mater 2009;57:549.
- [12] Martin CL, Camacho-Montes H, Olmos L, Bouvard D, Bordia RK. J Am Ceram Soc 2009;92:1435.
- [13] Olmos L, Martin CL, Bouvard D. Powder Technol 2009;190:134.
- [14] Wonisch A, Kraft T, Moseler M, Riedel H. J Am Ceram Soc 2009;92:1428.
- [15] Itahara H, Tani T, Nomura H, Matsubara H. J Am Ceram Soc 2006;89:1557.
- [16] Tikare V, Braginsky M, Bouvard D, Vagnon A. Comput Mater Sci 2010;48:317.
- [17] Wang Y, Liu Y, Ciobanu C, Patton BR. J Am Ceram Soc 2000;83:2219.
- [18] Wang YU. Acta Mater 2006;54:953.
- [19] Asp K, Ågren J. Acta Mater 2006;54:1241.
- [20] Shinagawa K. Steel Res Int 2010;81:1348.
- [21] Allen S, Cahn J. Acta Metall 1979;27:1085.
- [22] Cahn JW, Hilliard JE. J Chem Phys 1958;28:249.
- [23] Rahaman N. Ceramic processing and sintering: M. Dekker; 1995.
- [24] Svoboda J, Riedel H. Acta Metall Mater 1992;40:2829.
- [25] Elder KR, Grant M, Provatas N, Kosterlitz JM. Phys Rev E 2001;64:021604.
- [26] Fan D, Chen LQ. Acta Mater 1997;45:611.
- [27] Svoboda J, Riedel H. Acta Metall Mater 1995;43:1.
- [28] Bouvard D, McMeeking RM. J Am Ceram Soc 1996;79:666.
- [29] Pan J, Cocks ACF. Acta Metall Mater 1995;43:1395.
- [30] Pan J, Le H, Kucherenko S, Yeomans JA. Acta Mater 1998;46:4671.
- [31] Parhami F, McMeeking RM, Cocks ACF, Suo Z. Mech Mater 1999;31:43.
- [32] Bruchon J, Pino-Muñoz D, Valdivieso F, Drapier S. J Am Ceram Soc 2012;95:2398.